Eksploatacja i Niezawodnosc – Maintenance and Reliability

Volume 25 (2023), Issue 4

journal homepage: http://www.ein.org.pl

Article citation info:
Bayrak R, Sagirli A, Effect of different roller end-flange constructions on the fatigue life of the cylindrical roller bearings: A novel flange deformation formula, Eksploatacja i Niezawodnosc – Maintenance and Reliability 2023: 25(4) http://doi.org/10.17531/ein/174296

Effect of different roller end-flange constructions on the fatigue life of the cylindrical roller bearings: A novel flange deformation formula

Indexed by: Web of Science Group

Ramazan Bayrak[a,*], Ahmet Sagirli[a]

[a] Mechanical Engineering, Yildiz Technical University, Turkey

Highlights

- Novel formulas for the flange-roller end contact in the cylindrical roller bearings have been derived.
- Roller-raceway contact pressures have been obtained assuming elastic half-space model.
- The effect of different roller end-flange designs on fatigue life is investigated.
- Roller bearing with toroidal roller end-toroidal flange design has been seen having highest life.

Abstract

This paper performs the fatigue life analysis of the radial Cylindrical Roller Bearings (CRBs) with consideration of various roller end-flange shapes such as toroidal-toroidal, spherical-toroidal, and spherical-conical. A novel formula for each flange contact deformation in cylindrical roller bearing with different roller end-flange geometry including toroidal geometry is developed. Inner ring misalignment angle and radial deflection results obtained from the present study are verified with numerical and experimental results from the literature. The results approach to that of literature when the flange is changed from toroidal geometry to conical geometry. Using formulas developed in the present study, the effect of various roller end-flange geometries on the bearing life is investigated for different external loadings. It is observed that the bearing life increases when the roller end and flange are changed to toroidal geometry.

Keywords
cylindrical roller bearing, roller end-flange design, fatigue life, misalignment.

1. Introduction

In rolling bearing design, fatigue life has long been considered as a significant parameter [34]. For this reason, it is necessary to include all conceivable factors influencing bearing life when carrying out a more detailed fatigue life analysis. For the Cylindrical Roller Bearings (CRBs), the moment load, which causes ring misalignment, and the axial load exerted along the bearing's ring axis can be counted as the major external loading factors reducing the fatigue life. Besides the loading factors, the CRBs' performance is heavily influenced by the geometrical factors such as roller profile, internal bearing clearance, roller end-flange construction.

A moment load or a misaligned bearing ring and a bearing axial load (for NJ/NUP-type CRBs) can cause the roller to tilt and to occur non-continuous roller-race contact pressures, hence can affect the bearing life. Numerous studies have been conducted on the effect of external load conditions on the fatigue life of the roller bearings [3, 6, 10, 16, 21, 33, 34, 36]. The effect of ring misalignment on the fatigue life can be seen particularly in these studies. There are also many studies about the effect of roller profile (crowning) on the CRBs' fatigue life [25, 26, 29, 37]. Roller profile is a geometrical factor and nonuniform pressure occurs when this geometrical factor is not

(*) Corresponding author.
E-mail addresses: R. Bayrak, (ORCID: 0000-0001-6269-0834) rbayrak@yildiz.edu.tr, A. Sagirli (ORCID: 0000-0002-8840-8048) sagirli@yildiz.edu.tr

proper. Internal bearing clearance is another design (geometrical) factor that affects the bearing internal load distributions, hence the bearing life. Its effect on the bearing life has been a matter of study by some researchers [7, 27, 39].

Yet another geometrical parameter determining roller bearing performance is the roller end-flange geometry design. Many researchers focused on the effect of roller end-flange shape on the lubrication and on the bearing axial load carrying capacity. Some of them claimed, for the cylindrical roller bearing, an optimum roller end-flange construction (e.g., spherical-conical, spherical-spherical, toroidal-conical, toroidal-spherical) aiming to enhance axial load capacity and to prevent edge loading between the flange-roller end [2, 13, 30]. Some of them presented the results related to the axial load carrying capacity of the CRBs having spherical roller end-conical flange construction [4, 17, 23]. The effect of roller end-flange geometry on the tapered roller bearing performance in terms of lubrication was addressed in the literature [14, 15, 40]. The effect of roller end-flange geometry of the CRB under different axial loads on its lubrication condition was studied in the papers [18, 20]. Li and Wen [20] took two different roller end-flange shapes as conical-conical and spherical-conical into consideration and they stated that the flange angle plays a decisive role in the axial load carrying capacity of the CRB. Krzeminski-Freda and Warda [18] considered the spherical roller end-conical flange geometry, and studied the effect of flange angle on friction and lubricant film formation between roller end and flange under different axial loads. Additionally, Krzeminski-Freda and Warda [18] investigated roller tilt and skew angles depending on the flange angle. They indicated that the effect of the resulting skew angle due to the variation of the flange angle on the bearing performance may be negligible because of the small values of the flange angle.

Different from the studies mentioned above, there are also more up-to-date studies in the literature that incorporate roller end-flange design [5, 35, 38]. Wirsching et al. [38] investigated the effect of roller end-flange modifications of the tapered roller bearings (e.g. sphere-conical, sphere-toroidal, toroidal-toroidal) on the hydrodynamic pressure, lubricant gap, and friction coefficient. Bayrak and Sagirli [5] investigated the effect of flange angle (β) on the fatigue life of the NUP-type CRB having spherical roller end and conical flange. They considered different external loading conditions and indicated that the effect of variation in β on the life is apparent under combined radial load and misaligned ring and combined radial and high axial load. Wang et al. [35] include the effect of flange angle on the internal load distribution of the CRBs in their study, and evaluate it in terms of its effect on the fatigue life. As seen above, studies on the effect of roller end-flange construction on bearing internal load distribution and fatigue life are limited. Considering the fact that roller end-flange design has effect on roller tilt [5, 35], more comprehensive studies on the effect of roller end-flange design on bearing internal load distribution and bearing life should be brought to the literature.

To the best of our knowledge, no studies exist in the literature investigating the effect of various roller end-flange pair geometries (e.g. the pairs of toroidal- toroidal, toroidal - conical, and spherical-conical) on the fatigue life of CRBs. In this study, fatigue analysis of a CRB is carried out considering different types of roller end-flange pair design. The effect of the roller end-flange pairs such as toroidal- toroidal, toroidal-conical, and spherical-conical on the bearing life under different external loads is investigated. While some approaches and formulas for the deformation in the spherical roller end-conical flange contact exist in the literature [3, 5, 11, 16, 18, 22, 24], no flange deformation formulations was derived in the literature to be used for CRBs having toroidal roller end-toroidal flange geometry. In the current study, a new formula is derived for toroidal roller end-toroidal flange geometry, which is a function of various bearing external loads. Since four flanges exist in NUP-type CRB, which is studied in the present work, four novel formulas of flange-roller end contact deformation (or interpenetration) exist. With this new formula, flange deformations for different roller end-flange geometries such as spherical-conical, toroidal-conical, spherical-toroidal can also be simulated. Bearing internal load distribution are obtained using the slicing method. Contact pressures between rollers and races for the ISO life calculation [8] are calculated by elastic half-space method. Using the Matlab software, a code that can compute the bearing fatigue life versus given various inputs (e.g. different roller end-flange designs, flange angle, clearance, roller profile, and various external loading) has been developed. The calculations in the current study have been carried out by assuming dry contact in elastic limits, pure rolling, and non-

conformal contacts; friction, roller skewing, and structural deformation of the rings are deemed negligible.

2. Determination of bearing load distribution

CRBs having flanges on both the inner and outer rings such as NUP, NJ, NH, and NF types can also carry some degree of axial load besides high radial loads. Additionally, if a moment load causing the ring to misalign is applied to the ring, obtaining roller race contact loads may become much more complicated due to the roller end-flange interactions. In this work, A CRB of the NUP type is used, and the approach in de Mull, Vree, and Maas [24] is adopted to calculate roller-race contact loads.

Inner ring displacement vector ($\{\delta\}^T=\{\delta_y, \delta_x, \gamma\}$) and the load vector ($\{F\}^T=\{F_y, F_x, M\}$) vectors can be seen in Fig. 1. To calculate the displacement vector of the inner ring ($\{u\}^T=\{u_r, u_x, \theta\}$) which is on the "inner-ring cross-section reference point (P)" (called like that in [24]), inner ring displacement vector $\{\delta\}$, which is on the point "O", has to be multiplied by a transformation matrix $\{R\varphi\}$[5, 24] :

$$\{u\} = [R\varphi]\{\delta\} \tag{1}$$

$$[R\varphi] = \begin{bmatrix} cos\,\varphi & 0 & 0 \\ 0 & 1 & -r_p\,cos\,\varphi \\ 0 & 0 & cos\,\varphi \end{bmatrix} \tag{2}$$

where r_p is the bearing pitch (mean) radius, angle φ is the angular position of each roller relative to the reference roller.

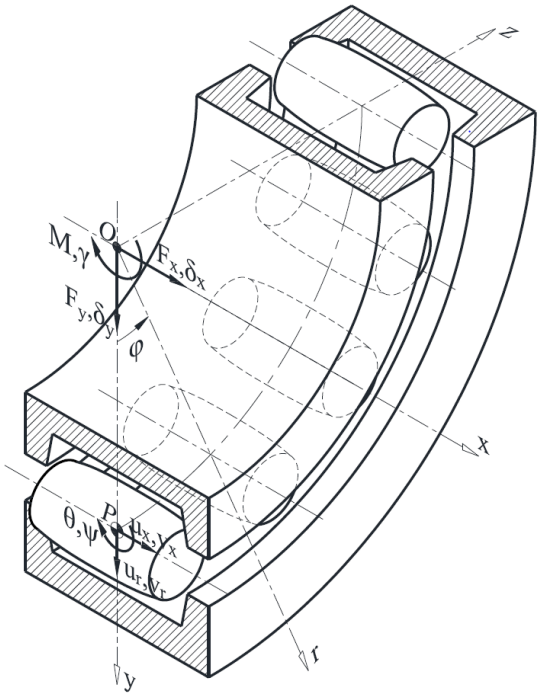

Fig. 1. Inner ring displacement $\{\delta\}$ and load $\{F\}$ vectors, and the displacement vectors $\{u\}$, $\{v\}$.

In Fig. 1, vector of $\{v\}^T=\{v_r, v_x, \psi\}$ is the displacement vector of the roller and is formed by the effect of the vector $\{u\}$. While there is a single displacement (δ) and load (F) vector of the inner ring, the vectors $\{u\}$ and $\{v\}$ are multiple as there is a cross-section reference point (P) at each roller position.

2.1. Roller-raceway contact loads

The contact loads between rollers and raceways are calculated by using the slicing method. The contact line is sliced into a sufficient number of slices and the contact loads and moments (Q_i, Q_o, T_i, T_o) are obtained by summing the loads on each slice (q_{ki}, q_{ko}), where the subscripts i, o, k denote inner race, outer race, and the k-th slice, respectively (Fig. 2). Formulations given in [24] are used to calculate the roller-race contact loads.

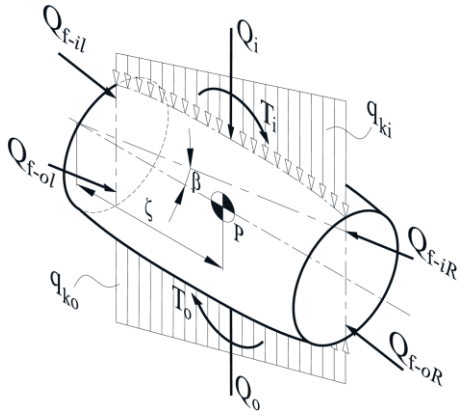

Fig. 2. Contact loads on a roller.

The contact load per unit length q_k for both inner and outer race can be obtained as follows [24]:

$$q_k = c\delta_k^{1.11} \tag{3}$$

where the contact deformation on the k-th slice is represented by "δ_k". The contact constant "c" was given in [3] as follows:

$$c = \frac{\pi E' l_e}{(7.358 l_e)^{1.11}} \tag{4}$$

where l_e, is effective contact length. E' is equivalent Young's modulus and is equal to $E'=E/(1-\nu^2)$ for the case of the contacting bodies being the same material, where ν is the Poisson's ratio. Contact deformation on the roller-inner race (δ_{ki}) and roller-outer race (δ_{ko}) are calculated as follows [24]:

$$\delta_{ki} = u_r - v_r + (\theta - \psi) \times l_k - h_k - P_d/4 \tag{5}$$

$$\delta_{ko} = v_r + \psi \times l_k - h_k - P_d/4 \tag{6}$$

where "l_k" stands for axial coordinate of each roller with respect to the roller center "P" (Fig. 2). "P_d" is internal radial clearance and "h_k" is the crown drop at the k-th slice. Considering the outer ring is fixed, (u_r-v_r) and v_r in Eqs. (5) and (6) represent the

deformations (or interpenetration) caused by translational motion of the roller and the rings in the local "r" direction. (θ-ψ) and ψ in Eqs. (5) and (6) respectively denote the relative angular displacements between the roller and the rings in local angular direction (Fig. 1). Logarithmic profile (h_k) given in the literature [7, 6, 19, 36, 37] is used in this work:

$$h_k(x) = 1.44 \times 10^{-4} D \left(\frac{h_m}{h_L}\right) ln \frac{1}{1 + e^{-g_K} - (2x/l_e)^{2\varepsilon_K}}$$

$$g_K = 4.66 - ln\frac{D}{l_e} \quad (7)$$

where "D" and "x" is the roller diameter and the axial coordinate of the roller-based roller center. The correction parameters h_m/h_L=3, ε_K=3 was employed in the literature to ensure that the rollers and races have the maximum contact capacity possible [36]. Contact loads "Q" and moments "T" is obtained by using all the Eqs. above [24]:

$$Q = \sum_{k=1}^{n_s} q_k \Delta l_k \quad (8)$$

$$T = \sum_{k=1}^{n_s} q_k l_k \Delta l_k \quad (9)$$

where "Δl_k" is the slice width at k-th slice.

2.2. The new formulas for the contact between toroidal roller end and toroidal flange

Assuming Hertzian point contact model, the contact load between roller end and flange can be calculated as follows [24]:

$$Q_f = c_f \delta_f^{3/2} \quad (10)$$

where c_f and δ_f are flange contact constant and flange contact deformation respectively.

As mentioned before, a formulation of the deformation between toroidal roller end and toroidal flange for roller bearings under different external loads does not exist in the literature. Therefore, a new formulation is derived in the present study with the help of 2D drawings. Assuming the radial (P_d) and axial (Δ_f) clearances exist, the initial positions of the roller and the rings before loading are shown in Fig. 3-a. Centers of each flange's curvature radius (f_{il}, f_{iR}, f_{ol}, f_{oR}) and of each roller end curvature radius (O_{il}, O_{iR}, O_{ol}, O_{oR}) can be seen in Fig. 3-a, where the subscripts i, o, l, R denote inner ring, outer ring, left side, right side. These are the centers of curvature radius in the drawing plane (plane "II"). There is one more principal plane (plane "I") which is perpendicular to the drawing plane. These planes are showed more clearly in Fig. 4. Each flange has its own local coordinate system: (x', r') for inner ring left side flange, (x, r') for inner ring right side flange, (x', r) for outer ring left side flange and (x, r) for outer ring right side flange (Fig. 3-a). When the inner ring and the roller move, which are the displacement vectors of the inner ring $\{u\}^T=\{u_r, u_x, \theta\}$ and the roller $\{v\}^T=\{v_r, v_x, \psi\}$ as mentioned before, curvature centers O_{il}, O_{iR}, O_{ol}, O_{oR}, f_{il}, f_{iR} are displaced with respect to their own local coordinate systems (Fig. 3-b). When the initial and final positions of the centers of curvature are known, all the necessary parameters for the force and moment equilibrium Eqs. can be calculated. These necessary parameters are: Flange deformation δ_f, the distance between the roller center and the point where flange contact intersects the roller center line ζ, and the angle between flange contact line and the roller center line after loading μ. These parameters are shown in Fig. 3-b for the *i*nner ring *l*eft side flange ($\delta_{f\text{-}il}$, ζ_{il}, μ_{il}). The procedure for obtaining these parameters is detailed below.

For the *i*nner ring *l*eft side, the initial coordinate of the center of roller end curvature radius which is in the drawing plane, plane II, O_{il} (x'_1 r'_1) is (Fig. 3-a):

$$x'_1 = (R_{re\text{I}} - R_{re\text{II}}) \times cos(\beta) - \zeta \quad (11)$$

$$r'_1 = (R_{re\text{I}} - R_{re\text{II}}) \times sin(\beta) \quad (12)$$

where $R_{re\text{I}}$ and $R_{re\text{II}}$ are the curvature radii on plane I which is perpendicular to drawing plane and plane II which is drawing plane, β is the angle of inclined flange, ζ is the distance between roller center and center of $R_{re\text{I}}$ (Fig. 3-a). The parameters of β, $R_{re\text{I}}$, $R_{re\text{II}}$, ζ are equal for four flanges. Subscript "re" symbolize the roller element. With the help of a vector L_{re} from the center of coordinate system to center of curvature radius $R_{re\text{II}}$ (Fig. 3-a), the final position of the curvature center can be found. At the initial position, the length of the vector $|L_{re}|$ and its angle with the x'-axis α_{re} are (Fig. 3-a):

$$|L_{re}| = \sqrt{(x'_1)^2 + (r'_1)^2} \quad (13)$$

$$\alpha_{re} = tan^{-1}(r'_1/x'_1) \quad (14)$$

In the similar way, for the inner ring left side, the initial coordinate of the center of flange curvature radius which is in plane II, f_{il} (x'_2 r'_2) is:

$$x'_2 = \left(R_{re\text{I}} + R_{f\text{II}}\right) \times cos(\beta) - \zeta + \Delta_f \quad (15)$$

$$r'_2 = \left(R_{re\text{I}} + R_{f\text{II}}\right) \times sin(\beta) + P_d/4 \quad (16)$$

where the Δ_f and P_d are axial and radial clearances respectively (Fig. 3-a). The initial length of the vector $|L_f|$ of the flange curvature and its angle with the x'-axis α_f are (Fig. 3-a):

$$|L_f| = \sqrt{(x'_2)^2 + (r'_2)^2} \quad (17)$$

$$\alpha_f = tan^{-1}(r'_2/x'_2) \quad (18)$$

The final positions of the curvature centers of roller end O_{il} (x'_3, r'_3) and flange f_{il} (x'_4, r'_4) are dependent on the displacement vectors of the roller $\{v\}^T=\{v_r, v_x, \psi\}$ and the inner ring $\{u\}^T=\{u_r, u_x, \theta\}$ respectively (Fig. 3-b):

$$x'_3 = |L_{re}| \times cos(\alpha_{re} + \psi) - v_x \quad (19)$$

$$r'_3 = |L_{re}| \times sin(\alpha_{re} + \psi) - v_r \quad (20)$$

$$x'_4 = |L_f| \times cos(\alpha_f + \theta) - u_x \quad (21)$$

$$r'_4 = |L_f| \times cos(\alpha_f + \theta) - u_r \quad (22)$$

The positive directions of $\{u\}$ and $\{v\}$ are shown in Fig. 3-a. The final distance "L" between the centers of roller end and flange curvatures in plane II (Fig. 3-b):

$$L = \sqrt{(x'_3 - x'_4)^2 + (r'_3 - r'_4)^2} \quad (23)$$

The *i*nner ring *l*eft side flange deformation $\delta_{f\text{-}il}$, which is one of the important parameters for the calculations, can be calculated with the help of the final distance L:

$$\delta_{f-il} = (R_{re\text{II}} + R_{f\text{ II}}) - L \quad (24)$$

where ($R_{re\text{II}}$+$R_{f\text{II}}$) is the distance between the curvature centers of roller end and flange in the initial contact position and can be seen more clear in Fig. 4. Another important parameter, as mentioned before, is the angle between flange contact line and the roller center line after loading μ:

$$\mu_{il} = tan^{-1}\left(\frac{r'_3 - r'_4}{x'_3 - x'_4}\right) - \psi \quad (25)$$

Yet another essential parameter is the distance between the roller center and the point where flange contact intersects the roller center line ζ_{il} after loading. The distance of ζ_{il} can be calculated by transferring the final coordinate points of the flange f_{il} (x'_4, r'_4) (or of the roller) to another local coordinate system of (x'', r'') (see Fig. 3-b). One can see this local coordinate system (x'', r'') in Fig. 3-b.

$$\begin{bmatrix} x''_4 \\ r''_4 \end{bmatrix} = \begin{bmatrix} cos(\psi) & sin(\psi) \\ -sin(\psi) & cos(\psi) \end{bmatrix} \begin{bmatrix} x'_4 + v_x \\ r'_4 + v_r \end{bmatrix} \quad (26)$$

Now that the angle μ_{il} and the transferred coordinates x''_4, r''_4 are known, ζ_{il} can be calculated:

$$\zeta_{il} = -\left(x''_4 - \frac{r''_4}{tan(\mu_{il})}\right) \quad (27)$$

The negative sign outside the parentheses in Eq. (27) is for the conversion of ζ_{il} to follow the sign convention in the roller moment equilibrium equation, which the clockwise is positive for the roller in Fig. 3.

If Fig. 3-b is taken as an example, the sign of the ζ_{il} will be minus with reference to local coordinate system (x'', r''). However, ζ_{il} must have positive sign according since the moment applied by the inner ring left side flange load around the roller center is expected to be clockwise. The new Eqs. (24), (25), and (27) are derived for *i*nner ring *l*eft side flange. Their expanded forms exist in Appendix as Eqs. (A1), (A5), and (A9). For other flanges, deformations $\delta_{f\text{-}iR}$, $\delta_{f\text{-}ol}$, $\delta_{f\text{-}oR}$, angles $\mu_{f\text{-}iR}$, $\mu_{f\text{-}ol}$, $\mu_{f\text{-}oR}$, and the distances $\zeta_{f\text{-}iR}$, $\zeta_{f\text{-}ol}$, $\zeta_{f\text{-}oR}$ can be derived by the same manner and not described for simplicity's purpose of the paper. They are also available in Appendix.

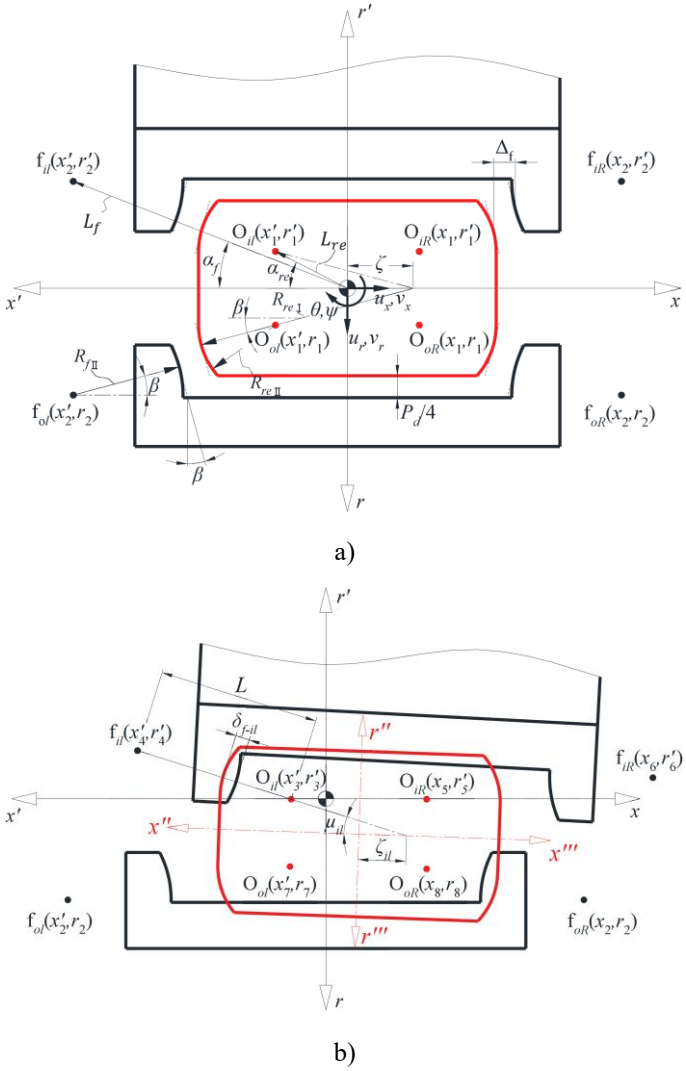

Fig. 3. The positions of the curvature centers of the roller end and flange (a) before loading (b) after loading.

2.3. Obtaining the curvature radii of the roller end and flange

In Fig. 4, the initial contact position of the roller end and flange is shown and the curvature radii in plane I and plane II can be seen more clear.

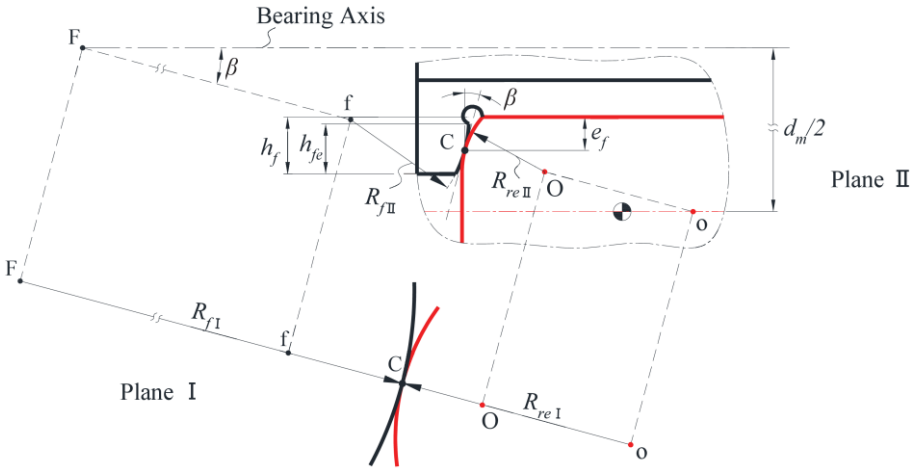

Fig. 4. The initial contact position of the roller end-flange geometry and their radii of curvatures.

In this study, $R_{re\mathrm{I}}$ is depended on the angle of inclined flange β. The relationship between $R_{re\mathrm{I}}$ and β is stated as follows [18]:

$$R_{re\,\mathrm{I}} = \left(D/2 - e_f\right)/\sin\beta \tag{28}$$

where D is the roller diameter and e_f is the contact point's radial distance from the raceway (see Fig. 4).

$$e_f = (1/2)h_{fe} + \left(h_f - h_{fe}\right) \tag{29}$$

where h_{fe} is the effective flange height, the difference between the total flange height h_f and the height of the undercut. The height of the contact point e_f is kept in the middle of h_{fe} as can be seen in Eq. (29). The curvature radii in plane I for the inner and outer ring flanges, R_{fI}:

$$R_{f\mathrm{I}} = \left((d_m/2)/\sin\beta\right) - R_{re\mathrm{I}} \quad for\ inner\ ring\ flange \tag{30}$$

$$R_{f\mathrm{I}} = \left((d_m/2)/\sin\beta\right) + R_{re\mathrm{I}} \quad for\ outer\ ring\ flange \tag{31}$$

The curvature radii in plane II (R_{fII},R_{reII}) are obtained as follows:

$$R_{re\mathrm{II}} = R_{re\mathrm{I}} \times k_{re} \tag{32}$$

$$R_{f\mathrm{II}} = R_{f\mathrm{I}} \times k_f \tag{33}$$

where k_{re} and k_f are the ratios of the curvature radius in plane II to that in plane I for the *r*oller *e*lement and *f*lange respectively. In this study, R_{fI} of inner ring flange (Eq. (30)) is used also for outer ring flange when calculating R_{fII}, which means R_{fII} is assumed to be equal for inner and outer ring flanges.

2.4. Obtaining of the flange contact constant c_f

After the flange contact deformation formulation has been derived δ_f, the contact constant c_f must also be calculated in order to calculate the flange load in Eq. (10). Expanding Eq. (10) :

$$Q_f = \left[\mathrm{F}\left(\left(\frac{4.5}{\varepsilon}\frac{1}{R}\right)\left(\frac{1}{\pi\kappa E'}\right)^2\right)^{1/3}\right]^{-3/2}\delta_f^{3/2} \tag{34}$$

Eq. (34) was given in the literature [9] for the Hertzian point contact models. Considering flange contact formula, Q_f=c_f×$\delta_f^{3/2}$, the term next to the $\delta_f^{3/2}$ in Eq. (34) corresponds to c_f. E' is equivalent Young's modulus, 1/R is the curvature sum of the flange and roller end with respect to two principal planes (plane I and plane II), which can be obtained using R_{fI}, R_{fII}, R_{reI}, R_{reII}. F and ε are the elliptic integrals of first and second kind, κ is the ellipticity. Approximate values of F, ε and κ were given in [9]:

$$\kappa = (R_{ratio})^{2/\pi} \tag{35}$$

$$\mathrm{F} = \pi/2 + (\pi/2 - 1)\,ln\,R_{ratio} \tag{36}$$

$$\varepsilon = 1 + (\pi/2 - 1)/R_{ratio} \tag{37}$$

where R_{ratio} is the ratio of effective radius of curvature in plane II to that in planeI, R_{ratio}=R_{II}/ R_{I}. Effective radii of curvature in plane II and plane I can be calculated for roller end-flange contact as:

$$1/R_{\mathrm{II}} = 1/R_{re\mathrm{II}} + 1/R_{f\mathrm{II}}\,,\quad 1/R_{\mathrm{I}} = 1/R_{re\mathrm{I}} + 1/R_{f\mathrm{I}} \tag{38}$$

2.5. Roller and bearing equilibrium equations

Force and moment equilibrium equations on a roller can be written as:

$$\begin{aligned} &Q_i - Q_o + \left(Q_{f-il} + Q_{f-iR}\right)\times\sin\beta \\ &\qquad - \left(Q_{f-ol} + Q_{f-oR}\right)\times\sin\beta = 0 \\ &\left(Q_{f-il} + Q_{f-ol}\right)\times\cos\beta - \left(Q_{f-iR} + Q_{f-oR}\right)\times\cos\beta = 0 \\ &T_i - T_o + \begin{pmatrix}\left(Q_{f-il}\times\sin(\mu_{il})\times\zeta_{il}\right)\\ +\left(Q_{f-oR}\times\sin(\mu_{oR})\times\zeta_{oR}\right)\end{pmatrix} - \\ &\begin{pmatrix}\left(Q_{f-iR}\times\sin(\mu_{iR})\times\zeta_{iR}\right)\\ +\left(Q_{f-ol}\times\sin(\mu_{ol})\times\zeta_{ol}\right)\end{pmatrix} = 0 \end{aligned} \tag{39}$$

First and second are the force equilibriums in radial and axial directions. Third one is the moment equilibrium equation on the roller. As in [24], the angle β which is the angle before loading is used in force equilibrium instead of the angle μ which is the angle after loading since its effect on the force equilibrium is small. The whole force (Q) and moments (T) on the roller can be also seen in Fig. 2. Definitions of all subscripts and the parameters of "μ" and "ζ" is made in the previous section. The non-linear Eqs. (39) are solved simultaneously for each roller to calculate the roller moves $\{v\}^{\mathrm{T}}=\{v_r,\ v_x,\ \psi\}$ by using the Newton-Raphson iterative method. Roller-race (Q_i, Q_o) and roller end-flange (Q_f) can be calculated after solving Eqs. (39).

The bearing equilibrium equations are derived for the inner ring and can be expressed as:

$$\{F\}+\sum_{j=1}^{Z}[R\varphi]^{T}\{Q_b\}_j=0 \tag{40}$$

where, $\{F\}^{\mathrm{T}}=\{F_y,\ F_x,\ M\}$, is the external load vector. "Z" is the total number of rollers, $\{Q_b\}_j$ is the inner ring contact load at the j-th roller position. Inner ring contact load $\{Q_b\}_j$ can be expressed as:

$$\{Q_b\}_j=\begin{Bmatrix} -Q_{ij}-(Q_{f-ilj}+Q_{f-iRj})\times \sin\mu_0 \\ (-Q_{f-ilj}+Q_{f-iRj})\times \cos\mu_0 \\ -T_{ij}-\left(Q_{f-ilj}\times sin(\mu_{ilj})\times\zeta\right)+\left(Q_{f-iRj}\times sin(\mu_{iRj})\times\zeta\right) \end{Bmatrix} \tag{41}$$

After solving Eqs. (39) by Newton-Raphson method, and obtaining all the contact loads, the bearing equilibrium equations (40) is solved by the same method to calculate inner ring displacements $\{\delta\}^{\mathrm{T}}=\{\delta_y,\ \delta_x,\ \gamma\}$.

3. Calculation of the contact pressures and fatigue life

Contact pressures between rollers and races are calculated by the elastic half-space method. Elastic deflection on the surface at any point due to a point load can be obtained by Boussinesq force-elastic deflection equation. The Boussinesq equation for a point load on the surface can be expressed as [32]:

$$w=\frac{F(1-\nu^2)}{\pi E r} \tag{42}$$

With this formula, the amount of elastic deflection "w" at a point on the surface that is distance "r" from the point load "F" can be calculated. "E" and "ν" are the Young's modulus and Poisson's ratio, respectively. As for contact area, infinite number of point loads arise, from which the contact pressure term shows up. Hence, Eq. (42) turns into integral term. With the help of Boussinesq force-elastic deflection equation, the following equation can be written for the non-conforming surfaces in contact [1, 34]:

$$K\int_{\Omega}\frac{p(x',y')dx'dy'}{\sqrt{(x-x')^2+(y-y')^2}}+z_1+z_2-(w_0+\alpha\times x)=0 \tag{43}$$

The integral term in Eq. (43) comes from Boussinesq equation (Eq. (42)) and represents the elastic deflection $w(x,y)$ at the point (x,y) generated by the normal pressure $p(x',y')$ at point (x',y'). "Ω" is denotes the region covered by the contact pressure, "z_1" and "z_2" are the profile functions of the contacting body bodies, "w_0" and "α" represent, respectively, bodies' relative translational and angular motions, "K" is the elastic parameter, and equals to $K=2\times(1-\nu^2)/(\pi\times E)$ for two bodies in contact that are made of the same material.

To solve Eq (43), the contact area can be discretized into small rectangular segments over which the constant pressure exist (Fig. 5).

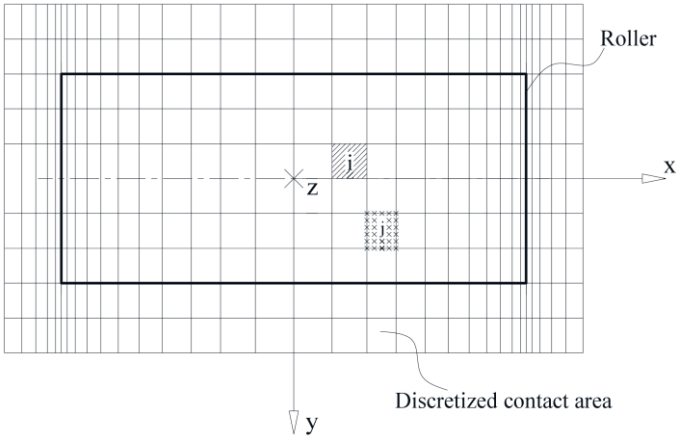

Fig. 5. Discredited contact area.

In the current study, discretization is done by using the rectangular segments of different sizes, the smaller rectangular segments are used at the roller ends to compute possible peak pressures more precisely and minimize computational effort (Fig. 5). After discretization has been applied to the integral term in Eq. (43), updated form of Eq. (43) is:

$$\sum_{j=1}^{n}p_j f_{ij}+z_{1i}+z_{2i}-(w_0+\alpha\times x_i)=0;i=1,2,3,\ldots,n \tag{44}$$

The literature defines "f_{ij}" as the influence coefficient that is the elastic deflection on the i-th segment due to the unit pressure on the j-th segment (p_j), and its formula can be found in the studies [1, 12]. One more equation is needed to obtain the contact pressures generated by the applied radial force:

$$Q-\sum_{j=1}^{n}A_j p_j=0;p_j>0 \tag{45}$$

Eqs. (44) and (45) are solved simultaneously to calculate the pressures on each segment (p_j), bodies' relative translational

motion (w_0), and actual contact area by using the Newton-Raphson method. The studies [1, 33, 34] contain the detailed process for solving Eqs. (44)-(45). Additionally, contact pressure calculation process in the present study is given in Fig. 6.

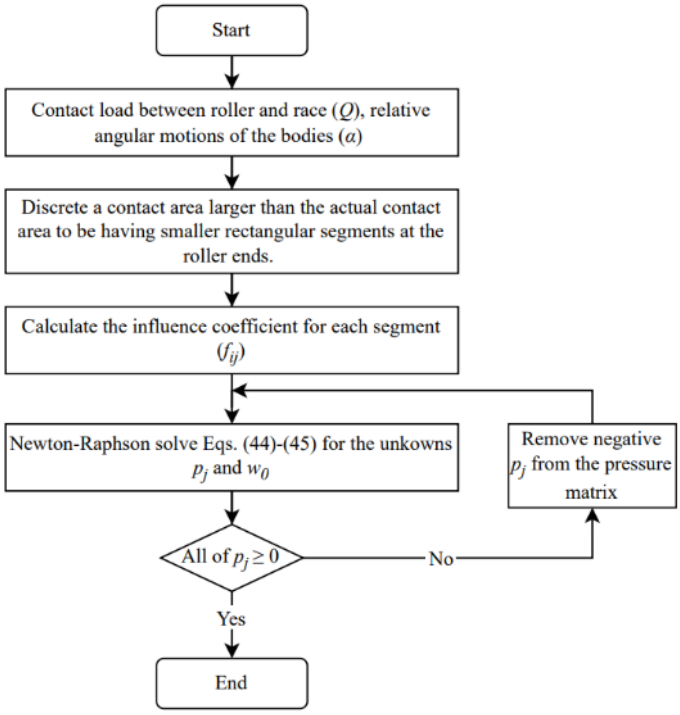

Fig. 6. Contact pressure calculation process.

To calculate the fatigue life of the CRB, the procedure in ISO [8] is employed in the current study. Assuming a 0.9 probability of survival, fatigue life of the CRB can be predicted as follows [8]:

$$L_{10r} = \left(\sum_{k=1}^{n_s} \left[\left(\frac{q_{c,ik}}{q_{e,ik}} \right)^{-4,5} + \left(\frac{q_{c,ok}}{q_{e,ok}} \right)^{-4,5} \right] \right)^{-\frac{8}{9}} \quad (46)$$

where n_s corresponds to the number of segments in the contact area's middle strip. Subscripts of k, i, o symbolize k-th segment at the middle strip, inner ring, outer ring, respectively. q_c and q_e are, respectively, the basic dynamic load rating and dynamic equivalent load of each segment at the middle strip of the contact (on the x-axis in Fig. 5). The parameter of q_c can be calculated as [8, 16]:

$$q_{c,mk} = Q_{c,m} \left(\frac{\Delta l}{l_e} \right)^{\frac{7}{9}} \quad (47)$$

where m is the inner race $m=i$ or the outer race m=o contact. Subscript of k represents the k-th segment and Δl is the k-th segment's length in the middle strip. Q_c is the basic dynamic capacity of the race and is stated as [8]:

$$Q_{c,m} = \frac{1}{\lambda v} \frac{C}{C_m Z} \left[1 + \left(1.038 \left(\frac{1-\chi}{1+\chi} \right)^{\frac{143}{108}} \right)^{\pm\frac{9}{2}} \right]^{\frac{2}{9}} \quad (48)$$

where m denotes the inner ring $m=i$ for upper sign, the outer ring $m=o$ for lower sign. For inner ring $C_m=C_i=0.378$, for outer ring $C_m=C_o=0.364$. Z is the number of rollers. The multiplication of λv is equal to 0.83, and "χ" is equal to (D/d_m) for the CRBs for the CRBs [8]. C is the basic dynamic radial load rating, and as follow for the single row CRBs:

$$C = b_m f_c l_e^{\frac{3}{4}} Z^{\frac{7}{9}} D^{\frac{29}{27}} \quad (49)$$

where b_m=1.1 for the present-day bearing steel. f_c is a parameter depending on the bearing geometry and material, and its formula can be found in ISO [28].

The dynamic equivalent load of each segment at the middle strip for each race ($q_{e,i}$, $q_{e,o}$) [8]:

$$q_{e,mk} = \left(\frac{1}{Z} \sum_{j=1}^{Z} \left(\left(\frac{p_{m,jk}}{271} \right)^2 \cdot D \cdot (1 \mp \chi) \cdot \Delta l \right)^{t_m} \right)^{\frac{1}{t_m}} \quad (50)$$

where the subscript m represents the inner race $m=i$ for upper sign, the outer race $m=o$ for lower sign. For the inner race $t_m=t_i=4$, for the outer race $t_m=t_o=4.5$. $p_{m,jk}$ denotes the contact pressures on the inner race $p_{i,jk}$ and outer race $p_{o,jk}$ in the location of the j-th roller and at the k-th segments (at the middle strip).

4. Results and discussions

4.1. Model verification

The approach in the reference study [24] is adopted in the present study to calculate bearing internal load distribution. However, in the current study, a new roller end-flange contact formulation is derived since NUP-type CRB having the toroidal roller end and the toroidal flange is studied. To verify this new formulation, numerical results from the present study and from the study [24] are compared. Experimental results in [24] are also compared with the results of current study. In [24], roller end-flange construction is spherical-conical (Fig. 7).

The given parameters in Fig. 7 are flange angle β=1°57', bearing pitch diameter d_m=72.5 mm, radial clearance P_d=0.02 mm, roller diameter ØD=14 mm, roller end sphere radius R_s=175 mm, effective roller length l_e=13.72, and Δ_a= 0.0015. In Fig. 7, the roller is partially crowned; straight part l_s=8.4 and arc radius R=604 mm. In the reference study [24], NUP-type CRB was studied numerically and experimentally. In the

experimental test rig, hydraulic radial force (F_y) between 0 and 20 [kN], and external moments (M_{ext}) of -8530, 0, and 4440 [Nmm] was applied to the bearing outer ring.

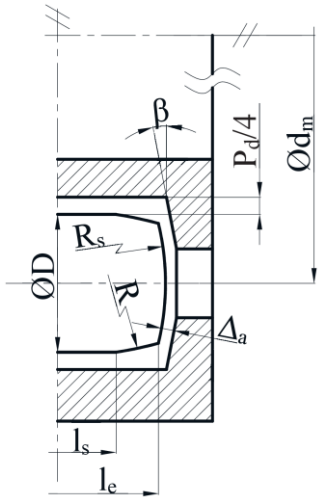

Fig. 7. The CRB geometry studied in Ref. [24].

Furthermore, the radial load was applied eccentrically e=0.2 [mm] and hence additional moment occurred (See Eq. (51)).

$$M = M_{ext} - \left(F_y - W\right) \times 0.2 \qquad (51)$$

where M is total moment applied and W is the static weight force and W=600 [N]. Because the test results of [24] had a low hysteresis, two curves exist for each test (Fig.8).

The outputs of inner ring misalignment angle γ and inner ring deflection δ_y are shown versus the inputs of different M_{ext} and F_y in Fig. 8(a) and Fig. 8(b), respectively. Triangles indicate the numerical results and dots indicate the experimental results of the reference study [24]. Different type of lines indicates the numerical results of the present study.

As mentioned above, conical flange-spherical roller end contact was assumed in the reference study [24]. Thus, in order to compare the results of the current study with those of the Ref. [24], the ratio of R_{fII}/R_{fI} is increased from 0.01 to 100 to simulate conical flange ($R_{fII}=\infty$), and the ratio of R_{reII}/R_{reI} is set as 1 to simulate spherical roller end.

As can be seen in Fig. 8-a, as R_{fII}/R_{fI} increases from 0.01 to 100, the numerical results of γ of the current study approach enough to numerical and experimental results of [24]. It can be deduced that the value of R_{fII}/R_{fI}=100 corresponds to $R_{fII} \cong \infty$ since the results overlap for the values of R_{fII}/R_{fI}=1 and R_{fII}/R_{fI}=100 (Fig. 8-a).

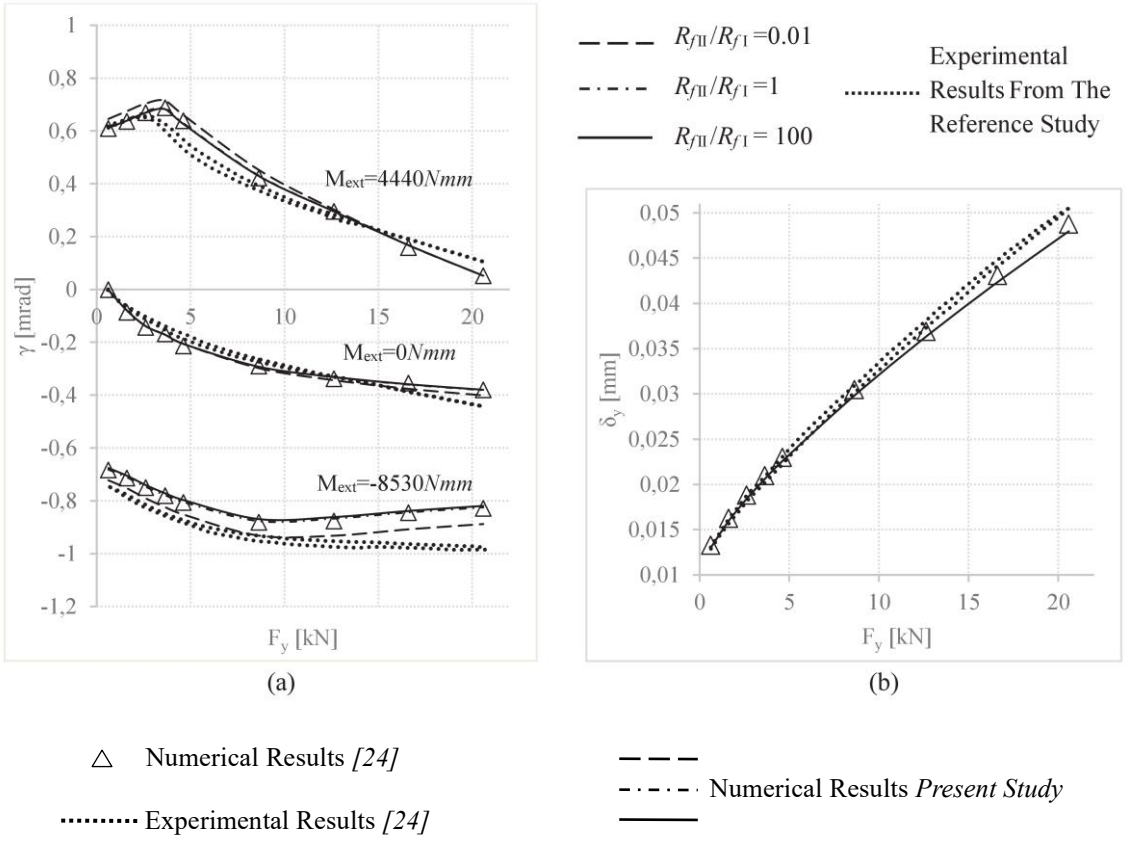

Fig. 8. Comparison of the results with those of the Ref. study [24] (a) ring misalignment angle γ, (b) ring deflection δ_y

Ring deflection (δ_y) are identical for different R_{fII}/ R_{fI} and for three external moments (Fig. 8-b). The insignificant differences between the results can be attributed to the difficulties encountered in replicating the graph with low resolution used in the work of [24].

The main verification of the present study is above mentioned numerical and experimental verification. Additionally, the novel formulas derived in the present study are compared and verified with the results measured in CAD drawings (See Appendix). This CAD verification is only a work of comparing formulas with their geometric equivalents.

4.2 Fatigue life results of the CRB under different external loads

In the current study, the effect of the ratios R_{reII}/ R_{reI} and R_{fII}/ R_{fI} on the fatigue life of a NUP type radial CRB is investigated for different external loads. In this work, radial load (F_y) and inner ring misalignment (γ) are considered as the external loads.

The combined loading F_y-γ is highly possible considering a shaft system on which a radial load is applied at the middle, and which is supported by a pair of CRBs. Table 1 contains the geometrical parameters and basic dynamic load rating (C) of the bearing. Some of the parameters listed in Table 1 are given in Refs. [6, 31]. As done in [24], the axial clearance ($2\times\Delta_f$) is kept minimal to investigate the influence of flange loads on the bearing load distribution. As mentioned before, R_{reI} and R_{fI} in Table 1 are dependent dimensions and are calculated according to Eqs. (28) and (30), respectively.

Table 1. The geometrical parameters and the dynamic load rating of the NUP-213 type CRB.

Parameter	*Value*
Pitch diameter, d_m [mm]	93.5
Roller mean diameter, D [mm]	15
Roller effective length, l_e [mm]	14
Total number of the rollers, Z	16
Total radial clearance, P_d [mm]	0.038
Total axial clearance, $2\times\Delta f$ [mm]	0.003
Flange angle, β [°]	0.5
Roller end curvature radius on plane I (R_{reI}) [mm]	661.7
Flange curvature radius of inner ring on plane I (R_{fI}) [mm]	4695.4
Dynamic load rating, C [kN]	122
Total flange height, h_f [mm]	2.95

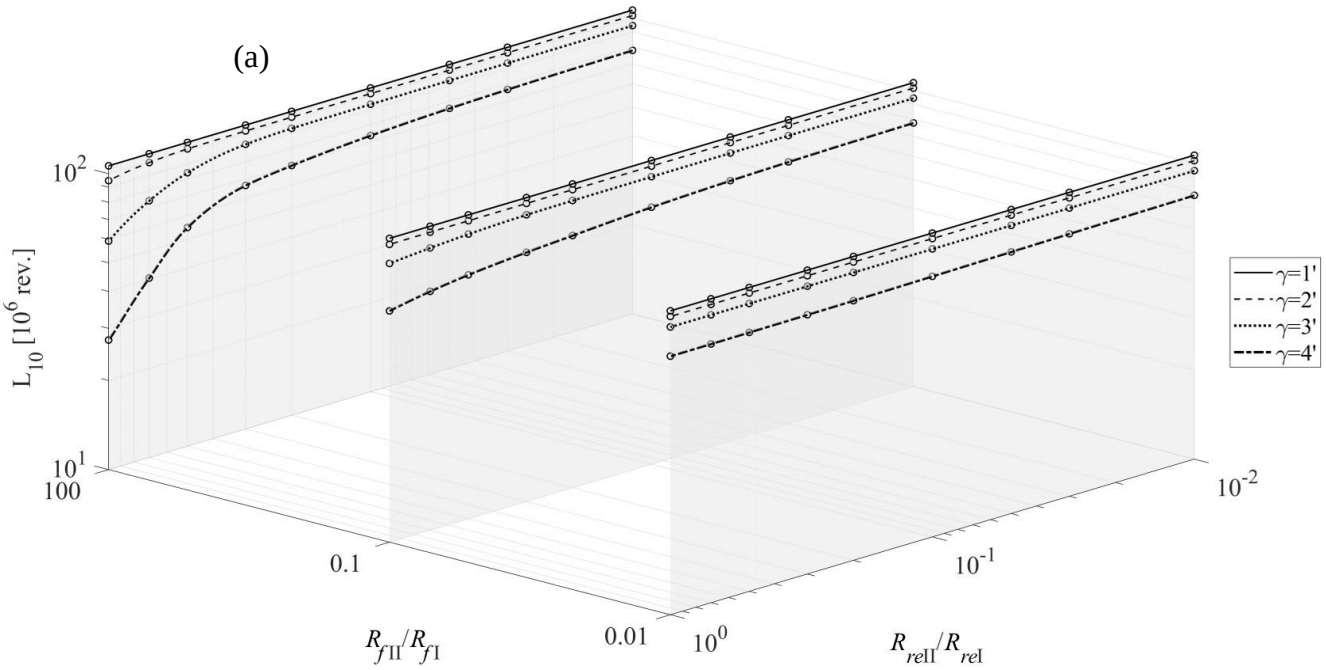

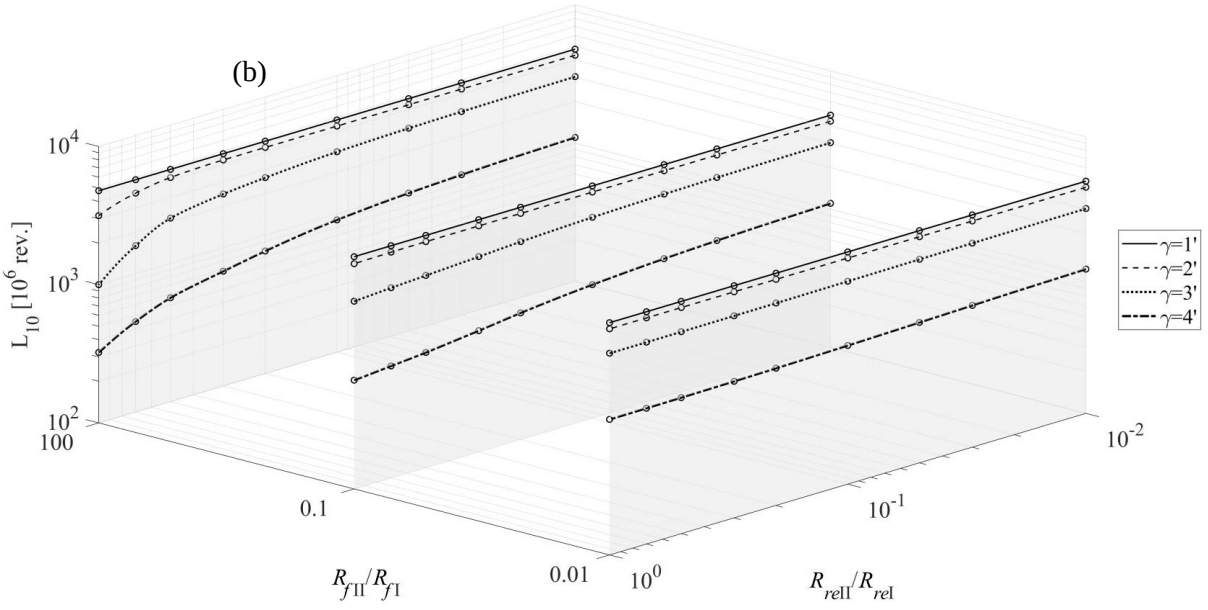

Fig. 9. Predicted fatigue life of the CRB for different ratios of R_{reII}/R_{reI} and R_{fII}/R_{fI}, and different misalignment angle of the inner ring (γ) (a) F_r=0.3C (b) F_r=0.1C.

Fig. 9 shows the bearing life results (L_{10}) against three variables: The ratios R_{reII}/R_{reI}, R_{fII}/R_{fI}, and inner ring misalignment angle (γ). For ease of perception, bearing radial load (F_y) is now referred to as "F_r". Fig. 9-a and b illustrate the fatigue life results for different radial loads F_r=0.3C=36.6 kN and F_r=0.1C=12.2 kN. As can be seen in Fig. 9, bearing life increases with decreasing ratios R_{reII}/R_{reI} and R_{fII}/R_{fI}. It is clear in Fig. 9 that the effect of the ratio R_{reII}/R_{reI} on the life is more dominant when R_{fII}/R_{fI}=100. It is worth reminding in here that R_{fII}/R_{fI}=100 corresponds to $R_{fII}\cong\infty$, which means inclined flat flange (conical flange). The main reason for the increase in the bearing life with the decrease of R_{reII}/R_{reI} and R_{fII}/R_{fI} is the decrease in contact stiffness c_f and thus decrease in flange loads Q_f.

In Fig. 10, flange contact loads are shown for each roller in the bearing having conical flange (R_{fII}/R_{fI}=100). Because of symmetry, nine rollers at 0-π diameter are given: Roller No. 1 at azimuth angle φ=0˚ (radially maximum loaded roller) and Roller No. 9 at azimuth angle φ=180˚. Decrease in the whole flange loads with decreasing ratio R_{reII}/R_{reI} can be seen in Fig. 10.

Considering the formula of the flange load, $Q_f=c_f\times(\delta_f)^{1.5}$, the main reason for the decrease in flange loads is that the flange contact constant (stiffness) c_f also decreases versus R_{reII}/R_{reI} (Fig. 11-a).

As can be seen in Fig. 11-a, as R_{reII}/R_{reI} decreases, the contact constant c_f which is the function of curvature radii decreases to a limit. This decrease of c_f (stiffness) reduces the flange loads (Fig. 10). When the flange loads decrease, the roller tilt ψ increases from a negative value to a positive limit (Fig. 11-b). Considering the sketch in Fig. 10-e, roller tilt is negative in that figure since the positive sign of the roller tilt is clockwise. When the roller tilt increases from negative to positive, interpenetration (deformation) of the roller and inner race decreases, hence the fatigue life increases to a limit (Fig. 9). Besides, as independent of the stiffness, since the decrease in R_{reII} also reduces the interpenetration (deformation) of bodies a little more, this geometric effect also contributes to the increase in fatigue life especially between R_{reII}/R_{reI}=1 and 0.1.

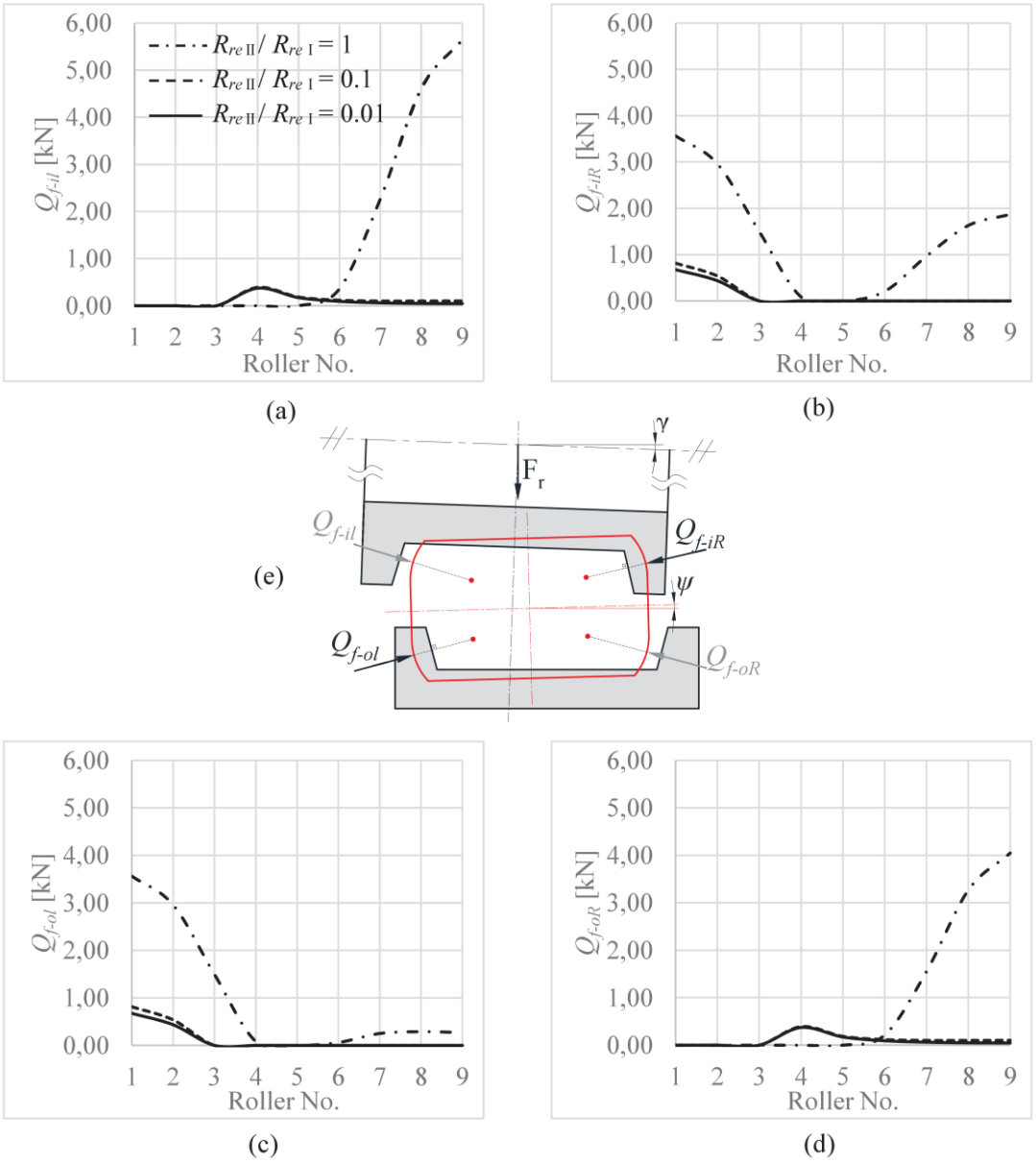

Fig. 10. Flange loads for all rollers in the bearing under F_r=0.3C and γ=4' (a)-(b) inner ring *l*eft side and *R*ight side flange loads $Q_{f\text{-}il}$ and $Q_{f\text{-}iR}$ (c)-(d) outer ring *l*eft side and *R*ight side flange loads $Q_{f\text{-}ol}$ and $Q_{f\text{-}oR}$ (e) a sketch showing flange loads for Roller No. 1.

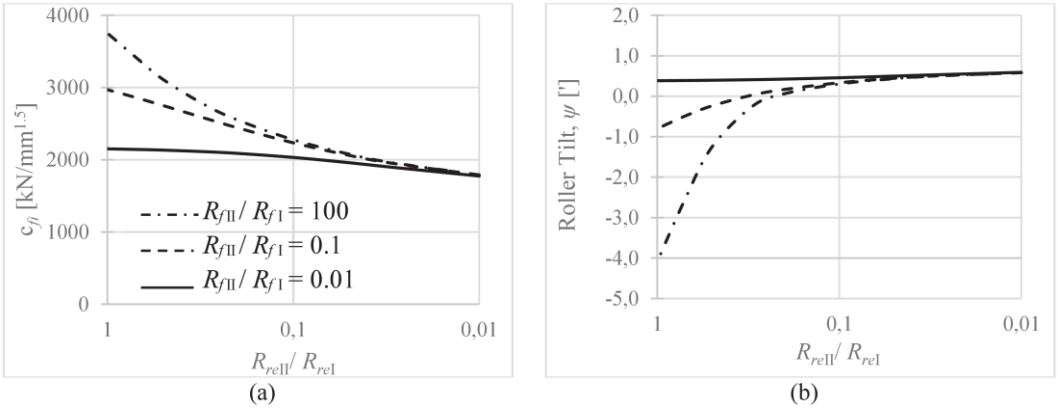

Fig. 11. (a) Variation of the flange contact constant (stiffness) of the inner ring versus $R_{reII}/\,R_{reI}$ and R_{fII}/R_{f1} (b) For F_r=0.3C and γ=4', the tilt angle ψ of the maximum loaded roller (Roller No. 1) versus $R_{reII}/\,R_{reI}$ and R_{fII}/R_{f1}.

5. Conclusions

Considering the effect of roller end-flange design on bearing internal load distribution and thus on bearing life and the scarcity of studies on this subject, the objective of the current study is to investigate the effect of different roller end-flange designs on the bearing life. In the present study, a novel formula for the deformation of each flange-roller end contact in the roller bearings has been derived as in Section 2.2, and their expanded forms for the whole flanges are given in the Appendix, Eqs. (A1-A4). In addition to these, new equations have been also derived for the parameters (μ and ζ) required for force and moment equilibrium equations on each roller (Eqs. A5-A12). Thereby, it is possible to investigate the effect of different roller end-flange geometries on the bearing load distribution, and hence on the life, by employing the flange contact deformation formula derived in this study. Although the cylindrical roller bearing is the research object of this study, this formulation derived in the present work can be also used for the tapered roller bearings. In this context, the studies carried out and the main results are summarized below:

(1) Different roller end-flange designs create different flange loads, hence affect the bearing internal load distribution. By considering this fact, the new formulas developed are validated by comparing the ring deflection and misalignment results of the present study with numerical and experimental results of [24]. The ratios R_{fII}/R_{fI} and R_{reII}/R_{reI} are adjusted to simulate the spherical roller end-conical flange pair which is studied in [24].

(2) By changing curvature radius ratios of flange (R_{fII}/R_{fI}) and the roller end (R_{reII}/R_{reI}), different flange-roller end designs (conical-spherical, toroidal-toroidal, toroidal-spherical) is obtained, and its effect on bearing load distribution and the fatigue life is investigated for combined load of F_r-γ. Fatigue life is calculated by using the method given in ISO [8].

(3) Since the ratios R_{reII}/R_{reI} and R_{fII}/R_{fI} affect the bearing load distribution, they affect the bearing life as well. Bearing life increases to a limit when the ratios R_{reII}/R_{reI} and R_{fII}/R_{fI} decreases. The main reason of this effect is that flange contact constant (stiffness) decreases to limit with decreasing ratios R_{reII}/R_{reI} and R_{fII}/R_{fI}. As the flange contact stiffness decreases, flange loads also decrease, which changes the roller tilt angle and increases the bearing life.

(4) In other words, the bearing life increases when the roller end is changed from spherical to toroidal geometry and the flange is changed from conical to toroidal geometry. Therefore, it is recommended to design the roller end and flange as toroidal geometry in order to achieve the best result in terms of bearing life.

(5) The effect of curvature radius ratio of roller end (R_{reII}/R_{reI}) on the predicted life is dominant when the flange has conical geometry (R_{fII}/R_{fI}=100≅∞). Similarly, the effect of the ratio of R_{fII}/R_{fI} on the life is dominant when the roller end is spherical geometry (R_{reII}/R_{reI}=1)

Acknowledgement

This paper is based on PhD thesis of the first author at Yildiz Technical University.

References

1. Ahmadi N, Keer L M, Mura T. Non-Hertzian contact stress analysis for an elastic half space-normal and sliding contact. International Journal of Solids and Structures 1983; 19(4): 357–373, https://doi.org/10.1016/0020-7683(83)90032-X.
2. Ai X. Roller Bearing With Enhanced Roller-End And Flange Contact. US Patent 10,428,870 B2 2019.
3. Andreason S. Load distribution in a taper roller bearing arrangement considering misalignment. Tribology 1973; 6(3): 84–92, https://doi.org/10.1016/0041-2678(73)90241-8.
4. Aramaki H, Cheng H S, Zhu D. Film thickness, friction, and scuffing failure of rib/roller end contacts in cylindrical roller bearings. Journal of Tribology 1992; 114(2): 311–316, https://doi.org/10.1115/1.2920889.
5. Bayrak R, Sagirli A. Fatigue life analysis of the radial cylindrical roller bearings roller end-flange construction effect. Mechanics Based Design of Structures and Machines 2022: 1–26, https://doi.org/10.1080/15397734.2022.2084751.
6. Chudzik A, Warda B. Fatigue life prediction of a radial cylindrical roller bearing subjected to a combined load using FEM. Eksploatacja i Niezawodnosc – Maintenance and Reliability 2020; 22(2): 212–220, https://doi.org/10.17531/ein.2020.2.4.

7. Chudzik A, Warda B. Effect of radial internal clearance on the fatigue life of the radial cylindrical roller bearing. Eksploatacja i Niezawodnosc – Maintenance and Reliability 2019; 21(2): 211–219, https://doi.org/10.17531/ein.2019.2.4.
8. DD ISO/TS 16281:2008. Rolling bearings - Methods for calculating the modified reference rating life for universally loaded bearings. Geneva, Switzerland, 2008.
9. Hamrock B J, Brewe D. Simplified Solution for Stresses and Deformations. J. of Lubrication Tech. 1983; 105(2): 171–177, https://doi.org/10.1201/9780203021187.ch17.
10. Harris T A. The Effect of Misalignment on the Fatigue Life of Cylindrical Roller Bearings Having Crowned Rolling Members. J. of Lubrication Tech. 1969; 91(2): 294–300, https://doi.org/10.1115/1.3554918.
11. Harris T A. Rolling Bearing Analysis. 4th ed. New York, John Wiley & Sons Inc: 2001.
12. Hartnett M J. The analysis of contact stresses in rolling element bearings. Journal of Tribology 1979; 101(1): 105–109, https://doi.org/10.1115/1.3453270.
13. Ijuin S, Yamamoto T. Cylindrical Roller Bearing. US Patent 6,530,693 B1 2003.
14. Jamison W E, Kauzlarich J J, Mochel E V. Geometric effects on the rib-roller contact in tapered roller bearings. ASLE Transactions 1977; 20(1): 79–88, https://doi.org/10.1080/05698197708982820.
15. Jiang X, Wong P L, Zhang Z. Thermal Non-Newtonian EHL Analysis of Rib-Roller End Contact in Tapered Roller Bearings. Journal of Tribology 1995; 117(4): 646–654, https://doi.org/10.1115/1.2831530.
16. Kabus S, Hansen M R, Mouritsen O. A new quasi-static cylindrical roller bearing model to accurately consider non-hertzian contact pressure in time domain simulations. Journal of Tribology 2012; 134(4): 1–10, https://doi.org/10.1115/1.4007219.
17. Korrenn H. The axial load-carrying capacity of radial cylindrical roller bearings. Journal of Tribology 1970; 92(1): 129–134, https://doi.org/10.1115/1.3451292.
18. Krzeminski-Freda H, Warda B. The effect of roller end-flange contact shape upon frictional losses and axial load of the radial cylindrical roller bearing. Tribology Series 1989; 14: 287–295, https://doi.org/10.1016/S0167-8922(08)70205-0.
19. Krzemiński-Freda H, Warda B. Correction of the roller generators in spherical roller bearings. Wear 1996; 192(1–2): 29–39, https://doi.org/10.1016/0043-1648(95)06739-6.
20. Li M, Wen S. The study of roller end and guiding shoulder construction of roller bearings. Tribology Series 1989; 14: 297–301, https://doi.org/10.1016/S0167-8922(08)70206-2.
21. Liu J Y. The Effect of Misalignment on the Life of High Speed Cylindrical Roller Bearings. J. of Lubrication Tech 1971; 93(1): 60–68, https://doi.org/10.1115/1.3451678.
22. Liu J Y. Analysis of Tapered Roller Bearings Considering High Speed and Combined Loading. J. of Lubrication Tech. 1976; 98(4): 564–572, https://doi.org/10.1115/1.3452933.
23. Morrison F R, Pirvics J, Crecelius W J. A functional evaluation of a thrust carrying cylindrical roller bearing design. Journal of Tribology 1979; 101(2): 164–169, https://doi.org/10.1115/1.3453304.
24. de Mull J M, Vree J M, Maas D A. Equilibrium and associated load distribution in ball and roller bearings loaded in five degrees of freedom while neglecting friction - part II: application to roller bearings and experimental verification. Journal of Tribology 1989; 111(1): 149–155, https://doi.org/10.1115/1.3261865.
25. Nagatani H. Fatigue Life Estimation for Roller Bearings Under Edge Load Occurrence. Transactions of the Japan Society of Mechanical Engineers Series C 2008; 74(742): 1609–1616, https://doi.org/10.1299/kikaic.74.1609.
26. Nagatani H. Improved method of roller bearing fatigue life prediction under edge loading conditions. Tribology Transactions 2010; 53(5): 695–702, https://doi.org/10.1080/10402001003699593.
27. Oswald F B, Zaretsky E V., Poplawski J V. Effect of Internal Clearance on Load Distribution and Life of Radially Loaded Ball and Roller Bearings. Tribology Transactions 2012; 55(2): 245–265, https://doi.org/10.1080/10402004.2011.639050.
28. PD ISO/TR 1281-1:2008. Rolling bearings — Explanatory notes on ISO 281, Part 1: Basic dynamic load rating and basic rating life. Geneva, Switzerland, 2008.
29. Poplawski J V., Zaretsky E V., Peters S M. Effect of Roller Profile on Cylindrical Roller Bearing Life Prediction. Cleveland, 2000. https://doi.org/10.1080/10402000108982466

30. Purdy G T. Rolling Bearings. US Patent 3,268,278 1966.
31. SKF. Rolling bearings PUB BU/P1 17000/1 EN. 2018.
32. Timoshenko S, Goodier J N. Theory of Elasticity. 2nd edition. New York, McGraw-Hill Company: 1951.
33. Tong V C, Hong S W. Fatigue life of tapered roller bearing subject to angular misalignment. Proceedings of the Institution of Mechanical Engineers, Part C: Journal of Mechanical Engineering Science 2016; 230(2): 147–158, https://doi.org/10.1177/0954406215578706.
34. Tong V C, Kwon S W, Hong S W. Fatigue life of cylindrical roller bearings. Proceedings of the Institution of Mechanical Engineers, Part J: Journal of Engineering Tribology 2017; 231(5): 623–636, https://doi.org/10.1177/1350650116668767.
35. Wang Z, Song J, Li X, Yu Q. Modeling and Dynamic Analysis of Cylindrical Roller Bearings Under Combined Radial and Axial Loads. Journal of Tribology 2022; 144(12): 1–12, https://doi.org/10.1115/1.4055406.
36. Warda B, Chudzik A. Effect of ring misalignment on the fatigue life of the radial cylindrical roller bearing. International Journal of Mechanical Sciences 2016; 111–112: 1–11, https://doi.org/10.1016/j.ijmecsci.2016.03.019.
37. Warda B, Chudzik A. Fatigue life prediction of the radial roller bearing with the correction of roller generators. International Journal of Mechanical Sciences 2014; 89: 299–310, https://doi.org/10.1016/j.ijmecsci.2014.09.015.
38. Wirsching S, Marian M, Bartz M et al. Geometrical optimization of the ehl roller face/rib contact for energy efficiency in tapered roller bearings. Lubricants 2021; 9(7): 1-19, https://doi.org/10.3390/lubricants9070067.
39. Yu A, Huang H Z, Li H et al. Reliability analysis of rolling bearings considering internal clearance. Journal of Mechanical Science and Technology 2020; 34(10): 3963–3971, https://doi.org/10.1007/s12206-020-2206-9.
40. Zhang Z, Qiu X, Hong Y. Ehl analysis of rib-roller end contact in tapered roller bearings. Tribology Transactions 1988; 31(4): 461–467, https://doi.org/10.1080/10402008808981849.

Appendix A

$$\delta_{f-il} = \left(R_{re\text{II}} + R_{f\text{ II}}\right) - \sqrt{\begin{matrix}\left[\left(|L_{re}| \times cos(\alpha_{re} + \psi) - v_x\right) - \left(\left|L_f\right| \times cos\left(\alpha_f + \theta\right) - u_x\right)\right]^2 \\ +\left[\left(|L_{re}| \times sin(\alpha_{re} + \psi) - v_r\right) - \left(\left|L_f\right| \times sin\left(\alpha_f + \theta\right) - u_r\right)\right]^2\end{matrix}} \quad \text{(A1)}$$

$$\delta_{f-iR} = \left(R_{re\text{II}} + R_{f\text{ II}}\right) - \sqrt{\begin{matrix}\left[\left(|L_{re}| \times cos(\alpha_{re} - \psi) + v_x\right) - \left(\left|L_f\right| \times cos\left(\alpha_f - \theta\right) + u_x\right)\right]^2 \\ +\left[\left(|L_{re}| \times sin(\alpha_{re} - \psi) - v_r\right) - \left(\left|L_f\right| \times sin\left(\alpha_f - \theta\right) - u_r\right)\right]^2\end{matrix}} \quad \text{(A2)}$$

$$\delta_{f-ol} = \left(R_{re\text{II}} + R_{f\text{ II}}\right) - \sqrt{\begin{matrix}\left[\left(|L_{re}| \times cos(\alpha_{re} - \psi) - v_x\right) - \left(\left(R_{rel} + R_{f\text{II}}\right) \times cos(\beta) - \zeta + \Delta_f\right)\right]^2 \\ +\left[\left(|L_{re}| \times sin(\alpha_{re} + \psi) - v_r\right) - \left(\left(R_{rel} + R_{f\text{II}}\right) \times sin(\beta) + P_d/4\right)\right]^2\end{matrix}} \quad \text{(A3)}$$

$$\delta_{f-oR} = \left(R_{re\text{II}} + R_{f\text{ II}}\right) - \sqrt{\begin{matrix}\left[\left(|L_{re}| \times cos(\alpha_{re} + \psi) + v_x\right) - \left(\left(R_{rel} + R_{f\text{II}}\right) \times cos(\beta) - \zeta + \Delta_f\right)\right]^2 \\ +\left[\left(|L_{re}| \times sin(\alpha_{re} + \psi) + v_r\right) - \left(\left(R_{rel} + R_{f\text{II}}\right) \times sin(\beta) + P_d/4\right)\right]^2\end{matrix}} \quad \text{(A4)}$$

$$\mu_{il} = tan^{-1}\left(\frac{\left[\left(|L_{re}| \times sin(\alpha_{re} + \psi) - v_r\right) - \left(\left|L_f\right| \times cos\left(\alpha_f + \theta\right) - u_r\right)\right]}{\left[\left(|L_{re}| \times sin(\alpha_{re} + \psi) - v_x\right) - \left(\left|L_f\right| \times cos\left(\alpha_f + \theta\right) - u_x\right)\right]}\right) - \psi \quad \text{(A5)}$$

$$\mu_{iR} = tan^{-1}\left(\frac{\left[\left(|L_{re}| \times sin(\alpha_{re} - \psi) - v_r\right) - \left(\left|L_f\right| \times sin\left(\alpha_f - \theta\right) - u_r\right)\right]}{\left[\left(|L_{re}| \times cos(\alpha_{re} - \psi) + v_x\right) - \left(\left|L_f\right| \times cos\left(\alpha_f - \theta\right) + u_x\right)\right]}\right) + \psi \quad \text{(A6)}$$

$$\mu_{ol} = tan^{-1}\left(\frac{\left[\left(|L_{re}| \times sin(\alpha_{re} - \psi) + v_r\right) - \left(\left(R_{rel} + R_{f\text{II}}\right) \times sin(\beta) + P_d/4\right)\right]}{\left[\left(|L_{re}| \times cos(\alpha_{re} - \psi) + v_x\right) - \left(\left(R_{rel} + R_{f\text{II}}\right) \times cos(\beta) - \zeta + \Delta_f\right)\right]}\right) + \psi \quad \text{(A7)}$$

$$\mu_{oR} = tan^{-1}\left(\frac{\left[\left(|L_{re}| \times sin(\alpha_{re} + \psi) + v_r\right) - \left(\left(R_{rel} + R_{f\text{II}}\right) \times sin(\beta) + P_d/4\right)\right]}{\left[\left(|L_{re}| \times cos(\alpha_{re} + \psi) + v_x\right) - \left(\left(R_{rel} + R_{f\text{II}}\right) \times cos(\beta) - \zeta + \Delta_f\right)\right]}\right) - \psi \quad \text{(A8)}$$

$$\zeta_{il} = -\left(\begin{pmatrix} \left[\left(\left|L_f\right| \times cos(\alpha_f + \theta) - u_x\right) + v_x\right] cos(\psi) \\ +\left[\left(\left|L_f\right| \times sin(\alpha_f + \theta) - u_r\right) + v_r\right] sin(\psi) \end{pmatrix} - \frac{\begin{pmatrix} -\left[\left(\left|L_f\right| \times cos(\alpha_f + \theta) - u_x\right) + v_x\right] sin(\psi) \\ +\left[\left(\left|L_f\right| \times sin(\alpha_f + \theta) - u_r\right) + v_r\right] cos(\psi) \end{pmatrix}}{tan(\mu_{il})} \right) \quad \text{(A9)}$$

$$\zeta_{iR} = -\left(\begin{pmatrix} \left[\left(\left|L_f\right| \times cos(\alpha_f - \theta) + u_x\right) - v_x\right] cos(-\psi) \\ +\left[\left(\left|L_f\right| \times sin(\alpha_f - \theta) - u_r\right) + v_r\right] sin(-\psi) \end{pmatrix} - \frac{\begin{pmatrix} -\left[\left(\left|L_f\right| \times cos(\alpha_f - \theta) + u_x\right) - v_x\right] sin(-\psi) \\ +\left[\left(\left|L_f\right| \times sin(\alpha_f - \theta) - u_r\right) + v_r\right] cos(-\psi) \end{pmatrix}}{tan(\mu_{iR})} \right) \quad \text{(A10)}$$

$$\zeta_{ol} = -\left(\begin{pmatrix} \left[\left(\left(R_{rel} + R_{fII}\right) \times cos(\beta) - \zeta + \Delta_f\right) + v_x\right] cos(-\psi) \\ +\left[\left(\left(R_{rel} + R_{fII}\right) \times sin(\beta) + P_d/4\right) - v_r\right] sin(-\psi) \end{pmatrix} - \frac{\begin{pmatrix} -\left[\left(\left(R_{rel} + R_{fII}\right) \times cos(\beta) - \zeta + \Delta_f\right) + v_x\right] sin(-\psi) \\ +\left[\left(\left(R_{rel} + R_{fII}\right) \times sin(\beta) + P_d/4\right) - v_r\right] cos(-\psi) \end{pmatrix}}{tan(\mu_{ol})} \right) \quad \text{(A11)}$$

$$\zeta_{oR} = -\left(\begin{pmatrix} \left[\left(\left(R_{rel} + R_{fII}\right) \times cos(\beta) - \zeta + \Delta_f\right) - v_x\right] cos(\psi) \\ +\left[\left(\left(R_{rel} + R_{fII}\right) \times sin(\beta) + P_d/4\right) - v_r\right] sin(\psi) \end{pmatrix} - \frac{\begin{pmatrix} -\left[\left(\left(R_{rel} + R_{fII}\right) \times cos(\beta) - \zeta + \Delta_f\right) - v_x\right] sin(\psi) \\ +\left[\left(\left(R_{rel} + R_{fII}\right) \times sin(\beta) + P_d/4\right) - v_r\right] cos(\psi) \end{pmatrix}}{tan(\mu_{oR})} \right) \quad \text{(A12)}$$

where $|L_{re}|$, α_{re}, $\left|L_f\right|$, and α_f in Eqs. (A1)-(A12) are:

$$|L_{re}| = \sqrt{\left(\left(R_{rel} - R_{reII}\right) \times cos(\beta) - \zeta\right)^2 + \left(\left(R_{rel} - R_{reII}\right) \times sin(\beta)\right)^2} \quad \text{(A13)}$$

$$\alpha_{re} = tan^{-1}\left(\left(\left(R_{rel} - R_{reII}\right) \times sin(\beta)\right) / \left(\left(R_{rel} - R_{reII}\right) \times cos(\beta) - \zeta\right)\right) \quad \text{(A14)}$$

$$\left|L_f\right| = \sqrt{\left(\left(R_{rel} + R_{fII}\right) \times cos(\beta) - \zeta + \Delta_f\right)^2 + \left(\left(R_{rel} + R_{fII}\right) \times sin(\beta) + P_d/4\right)^2} \quad \text{(A15)}$$

$$\alpha_f = tan^{-1}\left(\left(\left(R_{rel} + R_{fII}\right) \times sin(\beta) + P_d/4\right) / \left(\left(R_{rel} + R_{fII}\right) \times cos(\beta) - \zeta + \Delta_f\right)\right) \quad \text{(A16)}$$

In addition to the verification with experimental and numerical results from the literature, the results obtained from the above formulas are also verified by comparing them with the CAD drawings (see Table A1 and Table A2). In Table A1 and Table A2, the displacements given to the inner ring and roller can be seen (the combined loadings F_r-γ and F_r-F_a in Table A1 and Table A2, respectively). The results obtained by substituting the inner ring local deformation vector (u_r, u_x, θ) and the roller deformation vector (v_r, v_x , ψ) into the Eqs. (A1)-(A12) are compared with the results obtained from the CAD drawings. While the units of linear displacements (u_r, u_x, v_r, v_x) in Table A1 and A2 are mm, the units of angular displacements (θ , ψ) are degrees (◦). Inner ring and roller movements are given as a representation and are higher than the nominal values. Additionally, Fig. A1 is presented as a representation of the displacements of u_r=1, u_z=-1, v_r=0.5, v_z=-0.5, θ=1, ψ=-0.5.

Table A1. For the toroidal roller end (R_{reII}/ R_{reI}=0.01) and toroidal flange (R_{fII}/ R_{fI}=0.01), under F_r-γ combined loading, the results of roller end-flange deformation (δ), the angle of μ, and the distance of ζ against the inner ring and roller movements.

	u_r=2, u_z=-2, v_r=1, v_z=-1, θ=2, ψ=-1		u_r=1, u_z=-1, v_r=0.5, v_z=-0.5, θ=1, ψ=-0.5	
	CAD Drawing	Formula	CAD Drawing	Formula
$\delta_{f\text{-}iR}$	0.6636	0.6636	0.3434	0.3434
μ_{iR}	-3.6280	-3.6280	-1.5535	-1.5535
ζ_{iR}	-90.5703	-90.5703	-211.2169	-211.2169

	ur=2, uz=-2, vr=1, vz=-1, θ=2, ψ=-1		u_r=1, u_z=-1, v_r=0.5, v_z=-0.5, θ=1, ψ=-0.5	
	CAD Drawing	Formula	CAD Drawing	Formula
$\delta_{f\text{-}ol}$	0.8994	0.8994	0.4521	0.4521
μ_{ol}	-1.5859	-1.5859	-0.5386	-0.5386
ζ_{ol}	-206.9026	-206.9026	-608.5968	-608.5968

Table A2. For the toroidal roller end ($R_{re\text{II}}$/ $R_{re\text{I}}$=0.01) and toroidal flange ($R_{f\text{II}}$/ $R_{f\text{I}}$=0.01), under F_r-F_a combined loading, the results of roller end-flange deformation (δ), the angle of μ, and the distance of ζ against the inner ring and roller movements.

	u_r=2, u_z=2, v_r=1, v_z=1, θ=0, ψ=2		u_r=1, u_z=1, v_r=0.5, v_z=0.5, θ=0, ψ=1	
	CAD Drawing	Formula	CAD Drawing	Formula
$\delta_{f\text{-}il}$	0.7995	0.7995	0.4022	0.4022
μ_{il}	-2.5895	-2.5895	-1.0416	-1.0416
ζ_{il}	-126.8138	-126.8138	-314.8558	-314.8558
$\delta_{f\text{-}oR}$	0.7995	0.7995	0.4022	0.4022
μ_{oR}	-2.5895	-2.5895	-1.0416	-1.0416
ζ_{oR}	-126.8138	-126.8138	-314.8558	-314.8558

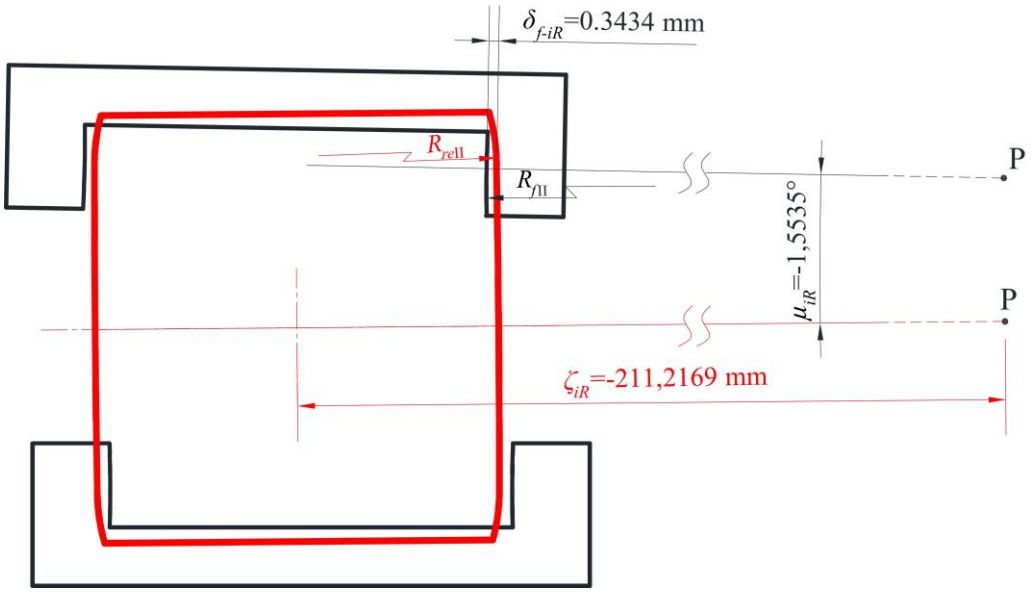

Fig. A1. CAD drawing and measured values for the displacements of u_r=1, u_z=-1, v_r=0.5, v_z=-0.5, θ=1, ψ=-0.5.